

Failure of load-bearing dyke networks as a trigger for volcanic edifice collapse

Samuel T. Thiele¹✉, Alexander R. Cruden² & Steven Micklethwaite³

Most large ocean-island volcanoes are gravitationally unstable. Some deform slowly, forming long-lived slumps, while others collapse and generate potentially dangerous debris avalanches. Here we investigate the effect of pervasive dyke networks on edifice instability, using data from La Palma, Spain. Like fibre-reinforced composites, where rigid layers are embedded in a compliant matrix, we find that dykes experience higher stress than surrounding host rocks. If the ratio of dyke to host stiffness is larger than the corresponding strength ratio, the dyke network will fail first, causing a rapid stress redistribution and possibly triggering edifice collapse. Fibre bundle models of a weak layer crosscut by dykes suggest this can occur with less seismicity or deformation than models without dykes. The models also suggest that dyke network strength could determine the potential for rapid collapse rather than gradual slump-type deformation. We conclude that dyke networks should be considered when assessing volcanic edifice stability.

¹Helmholtz Institute Freiberg, Helmholtz Zentrum Dresden Rossendorf, 09599 Freiberg, Germany. ²School of Earth, Atmosphere and Environment, Monash University, Melbourne, VIC 3800, Australia. ³Sustainable Minerals Institute, University of Queensland, Brisbane, QLD 4072, Australia. ✉email: s.thiele@hzdr.de

Unstable volcanic edifices exhibit a wide range of deformation styles and rates^{1,2}, which can be grouped into three categories: flank spreading, slumps and debris avalanches. Flank spreading, the largest-scale edifice instability, has been widely studied in Hawaii^{3–5} (USA). Weak sediments form a basal décollement along which volcanic flanks spread laterally due to edifice weight and internal magmatic pressure. The importance of volcano spreading is unclear within less active ocean-island volcanic complexes, such as the Canary Islands in the Atlantic and Réunion in the Indian Ocean^{6,7}. Volcanic slumps are slightly smaller scale features that form within many basaltic ocean-island volcanoes. These are generally bound by outward-dipping fault zones, such as the Hilina fault zone (Hawaii)⁴, and deform over relatively long time periods with deformation rates of <1 m/yr (although periods of rapid deformation can occur periodically)^{8,9}.

Unlike slumps and flank spreading, debris avalanches are short-lived and exceedingly energetic. This form of edifice instability was brought to the world's attention at Mount St. Helens (Washington, USA) in 1980 when 2.5 km³ of rock and ice collapsed to form a debris avalanche that travelled almost 30 km at up to 80 m/s¹⁰. Subsequently, debris avalanche deposits have been identified around many volcanoes^{11,12}, including most ocean-island volcanoes^{13,14}. It remains unclear why some instabilities evolve gradually (slumps) while others fail catastrophically (debris avalanches), and how likely slumps are to transition to catastrophic debris avalanches^{1,15}.

The infrequent but extreme impact of catastrophic edifice failures makes them difficult to incorporate into volcanic hazard assessments. This is especially so at large ocean-island volcanoes, where re-occurrence times can be hundreds of thousands of years, but the volumes of material involved can be as much as 5000 km³, potentially triggering devastating tsunamis^{16,17}. The risk posed by smaller island volcanoes is also significant, as demonstrated by Anak Krakatau (Indonesia) in 2018^{18,19}. Catastrophic edifice failures are challenging to predict due to the complexity of failure mechanisms involved, variety of preconditioning and triggering factors, and difficulty interpreting precursor signals such as deformation and seismicity¹.

Despite these difficulties, a variety of research highlights the importance of heterogeneity and specific weak regions formed by tuff or paleosol horizons^{20,21}, debris avalanche deposits²² or hydrothermal alteration^{23–25}. The shallow and often outward-dipping orientation of these layers allow shear strains to localise, so they dominate the overall stability problem; a laminate under layer-parallel shear is as strong as its weakest layer²⁶. The mechanically layered nature of volcanic edifices, generally defined by alternating lava flows, autoclastic breccias and/or pyroclastic deposits, has been widely acknowledged²⁷, and mechanical concepts from engineered composite materials have been applied to explain processes such as dyke arrest and fault propagation²⁸.

However, these studies all neglect a second significant source of mechanical variation: solidified sheet intrusions. These discordant structures have strength and stiffness values comparable to or larger than the strongest stratigraphic units²⁹, adding extra mechanical complexity and, we hypothesise, supporting a disproportionate amount of the total gravitational load by transmitting stress across weak layers.

Results

Field observations. La Palma, an ocean-island volcano in the western Canary Islands (Spain), last erupted in 2021³⁰, and has undergone at least two prehistoric catastrophic edifice collapses. The most recent of these occurred at ~550 ka³¹ and removed the south-western flank of the Volcán Taburiente edifice in one or more debris avalanches, with a total volume of ~95 km³ (based on

detailed bathymetry)¹⁴. The headwall of this collapse has since undergone significant erosional retreat, developing into the spectacular cliffs of Caldera Taburiente³¹, and providing a rare opportunity to investigate in detail the internal structure of a once-unstable volcano (Fig. 1).

Field traverses and uncrewed aerial vehicle (UAV) surveys³² allow us to make several key field observations on the mechanical structure of Volcán Taburiente. Firstly, large quantities of matrix-supported volcanic breccia are present immediately beneath the edifice, interpreted by previous authors as debris avalanche and scree deposits from an older (~1.2 Ma) collapse of the underlying Garafia edifice^{31,33}. These are potentially similar to the weak debris avalanche deposits (Mortalón) that have been identified on Tenerife (Canary Islands, Spain)³⁴. Welded phreatomagmatic tuff and scoria deposits in stratigraphic layers 10 s of metres thick also occur throughout the edifice²⁹, most abundantly within heavily intruded vent-proximal regions exposed in the north of Caldera Taburiente³² and along the Cumbre Nueva ridge (the remains of an axial rift zone associated with the late stages of the Taburiente edifice³¹, Fig. S1). UAV mapping³² and field traverses along the exceptionally well-exposed cliffs of Caldera Taburiente suggest that these deposits are generally not hydrothermally altered, a process often invoked at unstable “weak cored” volcanoes^{23,24}, at least within the (quite extensive) available exposures. We note, however, that these lithologies are likely to be mechanically incompetent even when unaltered^{21,35}.

Many thousands of dyke intrusions crosscut these pyroclastic and breccia layers^{29,32}. Estimates from the UAV surveys suggest that dykes occupy volume fractions of >10% close to the eruptive centre, and ~5% in more distal flanks³². Geological logging conducted during the construction of the LP-3 tunnel³⁶ through the Cumbre Nueva ridge shows extensive scoria deposits crosscut by up to 18% dykes (Supplementary Fig. 1). Well-developed dyke networks are also described in detail from Tenerife, where they have been interpreted to influence a significant (~5–10 km wide) region near the centre of the edifice, based on observations from water-mining tunnels³⁵.

These dykes form abundant mechanical discontinuities²⁹ that are significantly stiffer than the surrounding rocks (Fig. 2a; Table 1). We have also observed many 1–5 m long faults crosscutting these dykes (Fig. 2b–d), which we interpret to record a concentration of stress (due to the stiffness contrast between the dyke and surrounding host rock²⁹) that caused them to fail despite their strength (relative to the surrounding, largely intact, host rock). These intra-dyke faults have offsets of ~10–50 cm with kinematics consistent with compaction or gravitational sliding along bedding planes, and terminate close to the dyke margins. Importantly, these faults rarely propagate into the host rock.

We suggest that these observations provide evidence for a process analogous to material fatigue, in which relatively minor fracture growth compromises key load-supporting parts of a structure—potentially leading to rapid and catastrophic failure²⁶. In the following sections, we derive analytical and numerical models for this process and explore its possible implications on the development of volcanic edifice instabilities.

Intact rock properties. A Schmidt hammer was used to characterise the mechanical properties of the dykes, phreatomagmatic tuff and polymictic clast-supported breccia (clasts and matrix separately) at one of the sites where intra-dyke faults were observed (Hoyo Verde; Fig. S1). Rebound measurements (Table 1) were acquired using a Beton Rebound Hammer, which has a plunger with 25 mm diameter and 2.207 Nm impact energy, and repeated at least 15 times for each lithology. Dyke measurements were sampled from four different intrusions. These

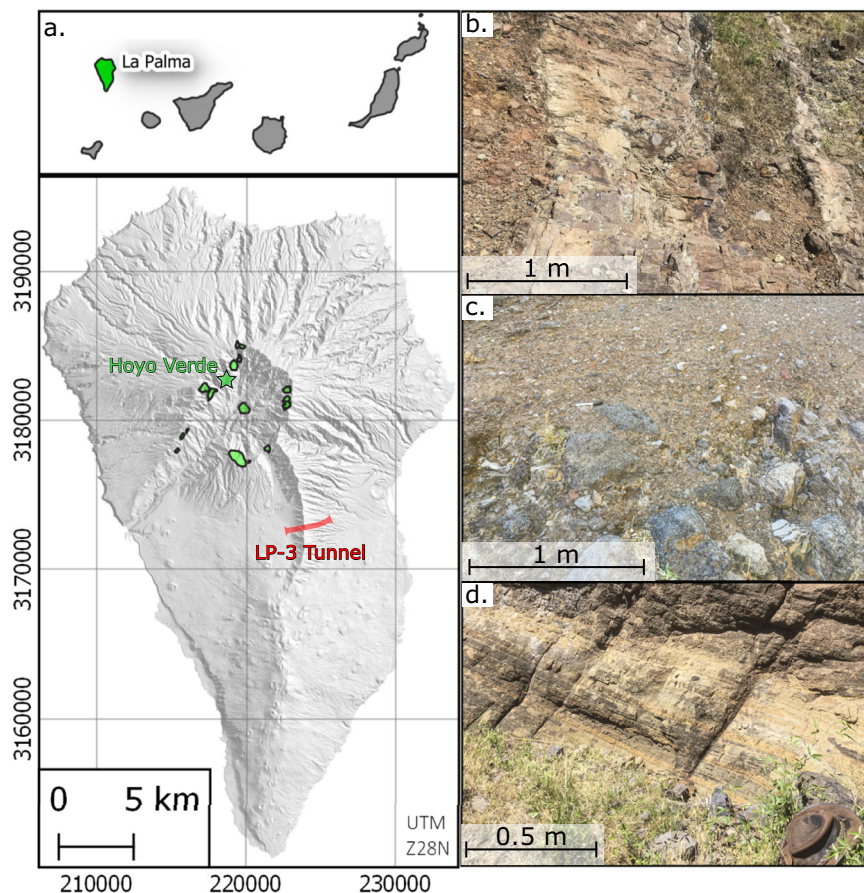


Fig. 1 Study area. Map of La Palma (a) showing the location of the uncrewed aerial vehicle (UAV) surveys (green polygons) from [32] and the LP-3 tunnel (red line). Field photos from Hoyo Verde (green star) show a typical dyke (b) and host-rock lithologies including a matrix-rich polymictic breccia (c) and phreatomagmatic tuff (d).

rebound measurements (R) were then used to estimate unconfined compressive strength (UCS) and Young's modulus (E), using the linear regression for basalts, andesites and tuffs derived by ref. 37, which have reported r^2 values of 0.95 and 0.85, respectively.

While these measurements give some indication of UCS and E , they are not statistically independent (both are derived from the same rebound measurement). Additionally, Figs. 3 and 5 from ref. 37 suggest that this regression somewhat overestimates both Young's modulus and UCS for tuffs, possibly explaining the relatively large values derived for the tuff at Hoyo Verde (Table 1).

Hence, we have supplemented the Schmidt hammer data by aggregating measurements of UCS and E for intact basalts and tuffs from ref. 38 and estimated properties for similar lithologies on Tenerife from ref. 21 and ref. 35 (Table 1). Based on these results, a UCS of 121 MPa and E of 20 GPa was selected as representative of intact basalt (dykes) and, 18 MPa and 4 GPa for intact tuff (weak host rock) at La Palma, although we note that considerable variation is likely in nature.

Rock-mass properties. It is well established that values for UCS and E derived from intact rock samples are significantly larger than equivalent values for rock masses^{39,40}, as both properties are reduced when fractures are present. The empirical Hoek-Brown⁴¹ and Hoek-Diederichs⁴² equations are widely employed to scale intact rock properties to fractured rock-mass properties, based on the geological strength index (GSI), a semi-

quantitative characterisation of rock-mass condition (fracturing and alteration).

Basaltic dykes are generally crosscut by cooling joints, and sometimes also margin-parallel fractures²⁹. Similar to³⁵ and³⁹ we thus use a GSI of 65 for upscaling the dyke properties. Published values for GSI in tuffs vary widely, from ~ 20 ³⁵ to ~ 80 ²¹, presumably due to highly variable degrees of welding between pyroclastic clasts. Noting that both the phreatomagmatic tuff and matrix-rich breccias we observed in La Palma are relatively well lithified, and locally fractured (Fig. 1), we use a GSI of 75 for these units. The Hoek-Brown equation requires an additional empirical parameter, mb , that we set as 10 for the host-rock (tuff) and 25 for the dykes, following values used for equivalent lithologies on Tenerife by ref. 21.

Micromechanics analysis. The structure of a weak layer crosscut by rigid dykes is mechanically similar to a fibre-reinforced composite, except that in our case the fibres (dykes) occupy an unusually low volume-fraction, compared to most engineered composites. Engineered composite materials comprise a matrix (e.g., epoxy) in which fibres or sheets (ply) of a stiffer or stronger material (e.g., glass or carbon) are embedded, resulting in bulk-mechanical properties that are drastically different to those of the pure constituents and can be optimised for a specific purpose²⁶. Similarly, volcanic rock masses can be mechanically very heterogeneous, often resulting in complex mechanical behaviour²⁸.

Adopting a micromechanics approach developed by the engineering community to model the behaviour of composite

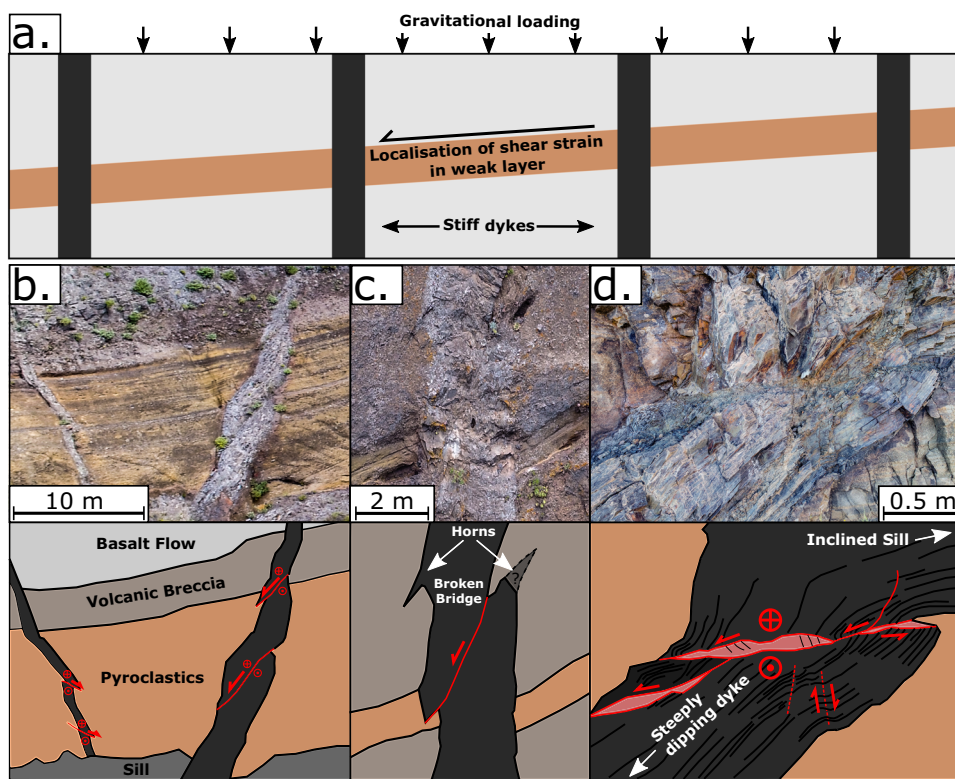


Fig. 2 Field observations. Conceptual model (a) and field observations (b-d) of faulted dykes in weak (pyroclastic tuff) host-rock layers. We interpret that the stiffness of the dykes causes stress concentration to the point of failure, analogous to the reinforcing fibres or membranes in a composite material. Similar small faults were observed in eight of seventeen dykes (47%) crosscutting a ~150 m long exposure of a single pyroclastic layer at Hoyo Verde (La Palma, Spain).

Table 1 Mechanical properties.

Lithology	Schmidt rebound (N)	Young’s modulus (GPa)		UCS (MPa)	
	(mm)	0.47 N-6.25	Literature	2.75 N-36.83	Literature
Intact basalt	49-63 (57)	16-23 (20)	17-21 (20) ³⁸ 6.6-19.8 ²¹	98-136 (121)	65-102 (82) ³⁸ 69-196 (99) ²¹ 100-250 (175) ³⁵
Breccia Clast	30-56 (49)	7-20 (16)		45-117 (97)	
Breccia Matrix	19-27 (23)	2-6 (4)	-1.1 ³⁴	15-37 (26)	-1.5 ³⁴
Tuff	33-38 (35)	9-11(10)	0.8-12 (4) ³⁸ 3.3-17.2 ³⁵	55-67 (60)	5-51 (18) ³⁸ 1-4 (2) ²¹ 4-27 (10.4) ³⁵
Basaltic rock mass		12.6		66	
Pyroclastic rock mass		3.3		22	

Summary of the mechanical properties of basaltic dykes and weak host-rock layers, based on Schmidt hammer measurements from La Palma³⁷ and published values for intact basalts and welded tuff^{21,35,38}. Values derived from the Schmidt hammer are the interquartile range and median (in brackets). Bold values were used to define intact rock properties for the subsequent upscaling and derive the rock-mass properties used for our modelling, as shown in the last two rows.

materials²⁶, we can solve for the internal shear stress within each material in a representative volume under imposed shear strain. Dykes can be lumped into a single “fibre” with a thickness that preserves the host-dyke volume fraction (Fig. 3a), assuming that both materials are isotropic and linear-elastic, and the shear stress σ_{yz} within each material calculated from its shear modulus G_{yz} and imposed shear strain ϵ_{yz} using Hooke’s law:

$$\sigma_{yz} = G_{yz}\epsilon_{yz} \tag{1}$$

These internal stresses, and the strength of each material, determine which material will fail first, and whether this failure will trigger a catastrophic failure of the composite. The critical

strain at which failure occurs can be calculated for each material:

$$\epsilon_{yz}^{A*} = \frac{\sigma_{yz}^{A*}}{G^A}, \text{ and } \epsilon_{yz}^{B*} = \frac{\sigma_{yz}^{B*}}{G^B} \tag{2}$$

if we assume the dykes (A) and host-rock (B) have yield stresses σ^{A*} and σ^{B*} , respectively (the peak shear stress above which rock failure results in fracturing and associated strength reduction). The material with the smaller critical strain will fail first: for A (dykes) to fail first, $\frac{\sigma_{yz}^{A*}}{G^A}$ must be less than $\frac{\sigma_{yz}^{B*}}{G^B}$. Following²⁶, the macroscopic stress $\hat{\sigma}_{yz}$ (large-scale shear stress) is the proportion (f) weighted average of the (micro)stresses in each

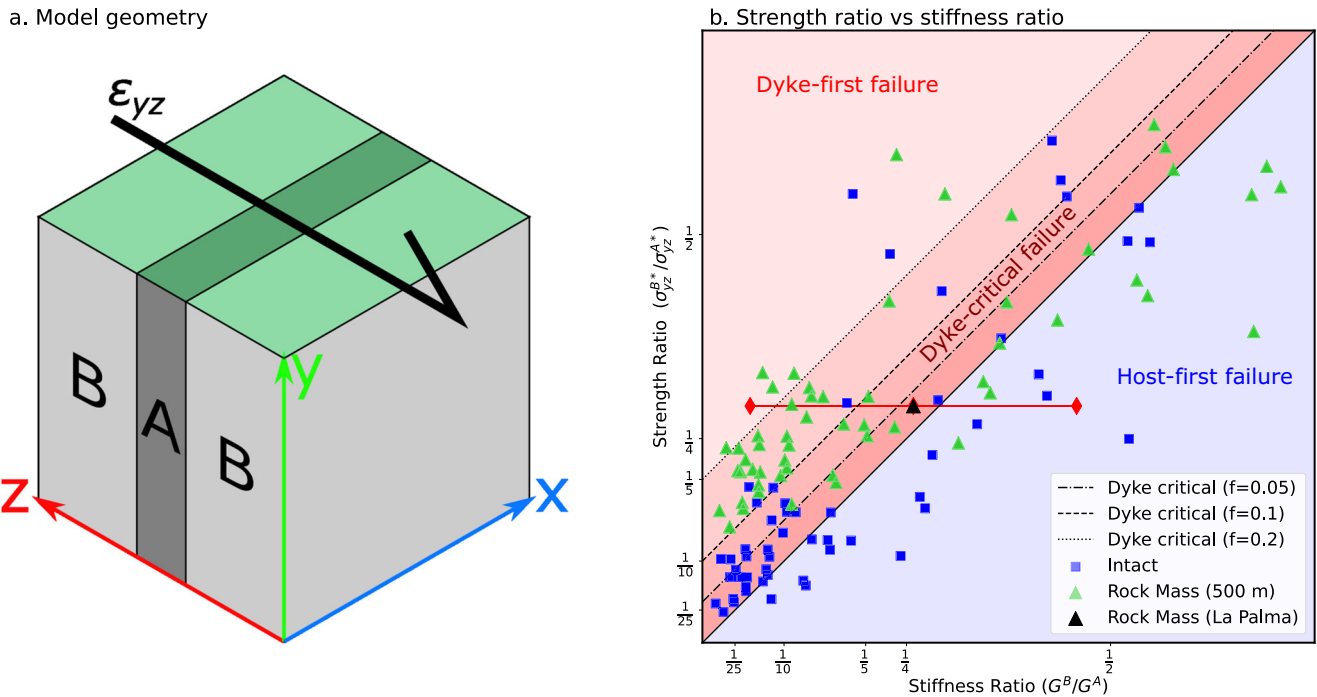


Fig. 3 Micromechanics. Micromechanical analysis of a dyke-host composite (a) showing (b) different predicted failure sequences. Blue squares in b show strength and stiffness ratios derived from random pairs of uniaxial compression test data for basalts and tufts compiled by³⁸. Green triangles show equivalent ratios using upscaled estimates of rock-mass properties based on these measurements (see text for details). Note that many of the intact and upscaled pairs are within the dyke critical regime, especially for areas with abundant dykes ($f > 0.1$). Our upscaled strength and stiffness values for La Palma (black triangle) are also within the dyke-critical regime, even for relatively small ($f = 0.05$) dyke fractions. The red bar shows the range of values used in the subsequent fibre bundle modelling.

material:

$$\widehat{\sigma}_{yz} = f\sigma_{yz}^A + (1 - f)\sigma_{yz}^B \quad (3)$$

where f is the volume fraction occupied by the dykes. Combining Eq. 2 and Eq. 3 (see Supplementary Methods), it is possible to predict which material will fail first under progressive loading and, significantly, if the remaining (non-failed) material can support this load on its own, or if a catastrophic failure occurs (Fig. 3b). This is best expressed using a criticality coefficient:

$$\frac{\sigma_{yz}^{B*}}{\sigma_{yz}^{A*}} - \frac{G_B}{G_A} = C_{crit} \begin{cases} C_{crit} \geq \frac{f}{1-f} : \mathbf{A} \text{ (dyke) fails first, but it is not catastrophic} \\ 0 < C_{crit} < \frac{f}{1-f} : \mathbf{A} \text{ (dyke) fails first, and it is catastrophic} \\ C_{crit} < 0 : \mathbf{B} \text{ (host rock) fails first} \end{cases} \quad (4)$$

This analysis, although highly simplified, highlights how dykes can determine the failure behaviour of a volcanic rock mass, even at low volume fraction, if the failure stress of each material (under the relevant confining conditions) is known. We have used intact measurements from³⁸ and the Hoek-Brown and Hoek-Diederichs scaling parameters described in the previous section to illustrate the range of plausible criticality coefficients (Fig. 3b) for rock masses crosscut by dykes at ~ 0.5 km depth ($\hat{\sigma}_3 \approx 4$ MPa). These result in a range of predicted behaviour, with a large number in the dyke-critical regime for dyke fractions of 0.05 to 0.2, including our best-estimate rock-mass properties for La Palma (black triangle). We have also validated these results by performing numerical experiments using the hybrid-discrete finite element software Irazu⁴³. These match our theoretical predictions (Supplementary Fig. 2).

Fibre bundle models. To further investigate the progressive failure of a weak layer crosscut by dykes, we have developed a simple fibre bundle model (FBM). FBMs have been widely

applied in statistical physics and materials engineering, where they have provided important insights into the damage and fracture of brittle materials⁴⁴⁻⁴⁶.

A traditional FBM comprises fibres that have stochastically distributed strengths and are collectively loaded under tension to failure. As weaker fibres break, the load is concentrated onto the remaining ones until eventually the whole bundle undergoes a catastrophic failure. In the lead-up to this event, non-critical failure cascades occur as the load-redistribution caused by one fibre yielding causes others to break.

Breakage cascades in FBMs are directly analogous to the acoustic emissions/seismicity observed in natural systems and, interestingly, also occur with power-law size-frequency distributions⁴⁷. As such, FBMs have been used to investigate a wide variety of natural phenomena, including force-chain development and collapse^{48,49}, rock fracture^{50,51}, earthquakes^{52,53}, landslides⁵⁴⁻⁵⁶, and avalanches⁵⁷. Significantly, it has been shown that the slope of the log cascade size-frequency distribution transitions from $-5/2$ to $-3/2$ as an FBM approaches global failure⁵⁸, leading some authors to suggest that insights from FBMs might help interpret precursor signals to predict large earthquakes and landslides^{51,55}.

The catastrophic collapse of a volcanic edifice to form a debris avalanche requires the flank to reach a threshold which induces a run-away weakening process. We take advantage of the ability of FBMs to simulate the progressive weakening and failure of non-homogeneous materials to further explore the role of load-bearing dyke networks in volcanic edifices.

Our model (Supplementary Methods) simulates the effect of dykes by introducing a fraction f of stiffer and stronger dyke-fibres, embedded within a bundle of weak and compliant host-fibres. The whole bundle is subject to increasing shear stress, and the resulting failure cascades and stress redistributions are

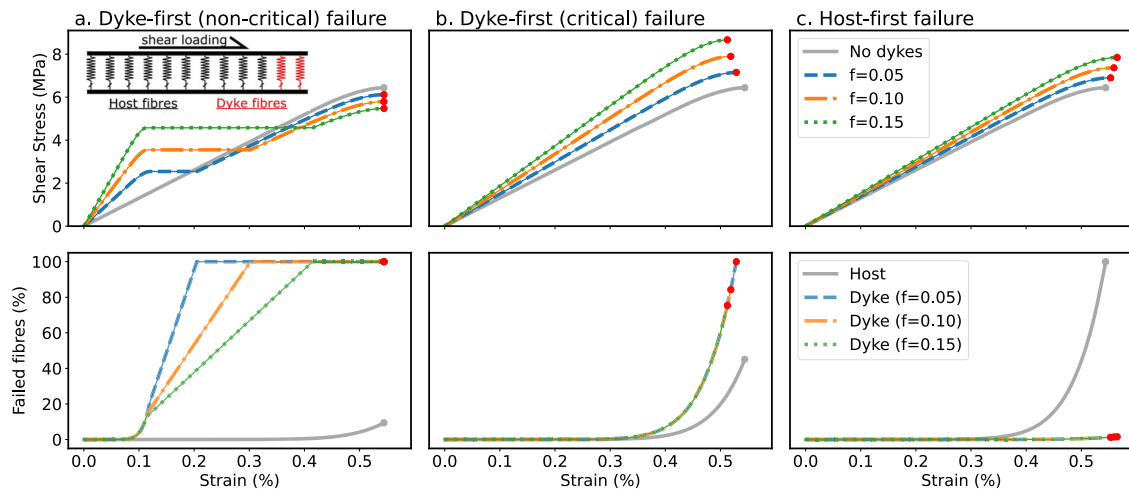


Fig. 4 Elastic fibre bundle models. Fibre bundle models for a weak layer under simple shear with 5%, 10% and 15% dyke fractions and dyke shear stiffness values of 22 (a), 5 (b) and 2.8 (c) GPa, as shown in Fig. 3b. These show varied failure-behaviour, as predicted by Eq. 4 and Fig. 3b: dyke-first but not critical failure (a), dyke-first and critical failure (b) and host-first failure (c). A model with no dykes (grey) is also plotted for reference. Host properties and dyke strength were kept constant, using the values outlined in Table 1. Dyke stiffness values were selected to match the red diamonds shown in Fig. 3b (a, c) and our best estimate for La Palma (b).

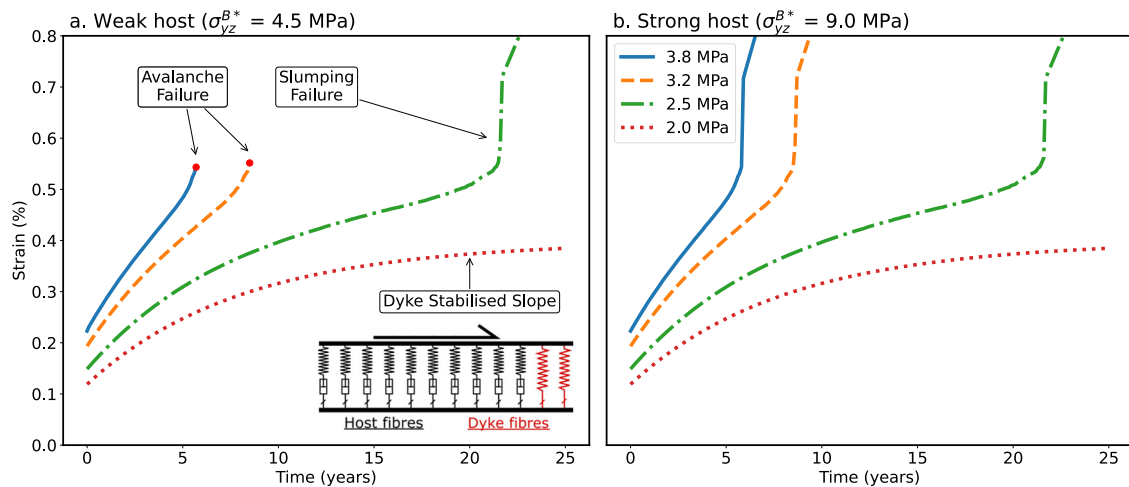


Fig. 5 Maxwell fibre bundle models. FBMs including inelastic (Maxwell) host-rock deformation that allows host stresses to dissipate over time. Viscous deformation of these host-fibres gradually transfers the load onto the dyke network, after which the models exhibit three possible behaviours: dyke-stabilised, catastrophic avalanche failure and slumping failure. Simulations were conducted with a weak host-rock (a) and using our estimated values for pyroclastic rocks on La Palma (b; Table 1) under various shear stresses (2.0–3.8 MPa) and a constant dyke fraction of 0.1.

recorded. Depending on the dyke shear stiffness, different behaviour emerges: Stiff dykes ($G = 22$ GPa) fail early, but the host does not (dyke-first non-critical failure; Fig. 4a). Intermediate dyke stiffness ($G = 5$ GPa), corresponding to our best estimate of dyke stiffness at La Palma (Fig. 3b), results in failure of the dyke network at shear stress exceeding the strength of the surrounding host rock, causing a cascading dyke-first critical collapse (Fig. 4b). Finally, more compliant dykes ($G = 2.8$ GPa) fail after surrounding host rock (host-first failure; Fig. 4c).

Compared to a control model containing no dykes, the dyke-critical model (Fig. 4b) fails with less precursor deformation and fewer failure cascades (Supplementary Fig. 3). As expected for FBMs⁴⁷, the distribution of fibre failures follows a power law with slope $-5/2$ (Supplementary Fig. 3).

Weak layers controlling the development of flank instabilities are also expected to undergo inelastic deformation^{20,59,60}, which can be partially incorporated into our FBM by using a Maxwell visco-elastic rheology that allows stresses in the host-rock fibres to dissipate over time. The dyke-fibres remain linear-elastic, since

solidified dykes are unlikely to undergo substantial viscous deformation at shallow depths. Viscous deformation of the host-fibres thus progressively transfers load onto the dyke network, exaggerating the initial stress concentration caused by their different stiffness.

Eventually, this load transfer progresses to the point where three possible outcomes emerge. Either (1) the dyke network is strong enough to stabilise the slope, akin to rock bolts in an unstable excavation; (2) the dykes break and transfer load back onto the host rock, causing a creeping landslide or; (3) the dykes fail and the host can no longer support the load, resulting in a catastrophic collapse. Our modified FBM models, although highly simplified, illustrate these various behaviours (Fig. 5). Avalanche failure is predicted for larger shear stresses if there is a significant strength difference between the dykes and the host rock (Fig. 5a), while slumping failures occur when the host rock is stronger (Fig. 5b) or the shear stress lower (Fig. 5a). The smallest applied shear stress resulted in a dyke-stabilised slope under both strong and weak host-rock scenarios.

Discussion

Our field observations and modelling results indicate that dyke networks can form a load-bearing framework that influences volcano edifice stability, possibly providing the cascading instability required to initiate catastrophic debris avalanches. If weak stratigraphic layers deform visco-elastically then the dyke network may also determine whether the system evolves into a stable, slumping or catastrophic state. We suggest that dyke networks increase the criticality⁶¹ of the volcanic edifice: while they comprise a small part of the system (5–20%), they concentrate stress and are highly interconnected, meaning the overall stability can depend on relatively few dykes. Under progressive loading or ductile stress transfer, the system evolves towards a critical state where a minor increase in stress can trigger a cascading failure, and thus a rapid transition from stable to very unstable.

As highlighted by the simulated loading curves in Fig. 4b, the model containing dykes failed more rapidly (at lower strain and with less precursor fibre breakages) than the control model. We ascribe this to the limited amount of fracturing (and hence seismicity) required to break the dyke network and reduce the bulk strength, meaning the critical point can be reached with limited warning. Regardless, increasing deformation and the change in power-law predicted by FBM models⁵⁸ still occurs, suggesting that prediction from monitoring data may be possible.

Furthermore, as shown in Figs. 2 and 4, the role of the dyke network in bulk failure can, in theory, be predicted based on the elastic moduli, strength, viscosity and volume fractions of the weakest stratigraphic layers and the dyke network. These values could be measured on samples collected in the field, or reasonably estimated by analogy to other similar volcanic systems, and used to determine whether dykes should be included in volcano stability analyses. Measurements from La Palma^{29,32} and the observations presented in Fig. 3 suggest that Volcán Taburiente (and other heavily intruded edifices elsewhere in the Canary Islands, Cape Verde Islands, Azores and La Réunion) could have failed in the dyke-critical domain. Similarly, solidified dykes are expected to be relatively insignificant for edifices where they are a minor portion (<5%) of the edifice (e.g., Krakatau, Mount St. Helens), or are highly focussed along discrete rift zones (e.g., Kilauea, Hawaii, USA).

Finally, our observation that Volcán Taburiente could have developed a weak core due to primary volcanological processes could be relevant at other large basaltic edifices. Relatively compliant pyroclastic deposits (scoria and tuff) are more abundant near eruptive vents (e.g., Fig. S1), potentially resulting in a primary “weak-core” structure when volcanic vents are focused into discrete zones, such as the “dorsal” ridges observed in the Canary Islands⁶² (Fig. S1). These zones may also be more susceptible to hydrothermal alteration, which could further exaggerate any primary differences. Simultaneously, the density of eruptive vents implies a concentration of crosscutting dykes in the subsurface, making it more likely that the cores of these volcanoes will be in the dyke-critical regime.

We conclude that dyke networks should be considered when evaluating the deformation and stability of volcanic edifices if dyke abundance is thought to exceed ~5%. Dyke networks can ideally be observed in outcrops and excavations, or inferred by analogy to other similar volcanoes. Measurements of their abundance and mechanical properties can then be used to derive non-linear, rock-mass scale, stress–strain relationships, such as our FBM results in Fig. 4, which can then be used in large-scale continuum models assessing volcano deformation and flank stability.

Data availability

The UAV data used in this study is available at <https://doi.org/10.26180/5d688c17f2ed2>. Our Schmidt hammer data and Irazu modelling results can be found at https://github.com/samthiele/dyke_network_failure.

Code availability

Python code for the derivation and scaling of rock mechanical properties and fibre bundle modelling is available as a Jupyter notebook at https://github.com/samthiele/dyke_network_failure. This includes the codes used to create Figs. 3–5 (<https://doi.org/10.5281/zenodo.8374275>).

Received: 5 December 2022; Accepted: 6 October 2023;

Published online: 18 October 2023

References

- McGuire, W. J. Volcano instability: a review of contemporary themes. *Geol. Soc. Lond. Spec. Publ.* **110**, 1–23 (1996).
- Keating, B. H. & McGuire, W. J. Island edifice failures and associated tsunami hazards. *Pure Appl. Geophys.* **157**, 899–955 (2000).
- Borgia, A. Dynamic basis of volcanic spreading. *J. Geophys. Res. Solid Earth* **99**, 17791–17804 (1994).
- Denlinger, R. P. & Morgan, J. K. Instability of Hawaiian volcanoes. in *Characteristics of Hawaiian Volcanoes*. Professional Paper 1801-4. <http://pubs.er.usgs.gov/publication/pp18014> (USGS Publications Warehouse, 2014).
- Morgan, J. K., Moore, G. F., Hills, D. J. & Leslie, S. Overthrusting and sediment accretion along Kilauea’s mobile south flank, Hawaii: Evidence for volcanic spreading from marine seismic reflection data. *Geology* **28**, 667–670 (2000).
- Münn, S., Walter, T. R. & Klügel, A. Gravitational spreading controls rift zones and flank instability on El Hierro, Canary Islands. *Geol. Mag.* **143**, 257–268 (2006).
- McGovern, P. J. et al. Lithospheric flexure and volcano basal boundary conditions: keys to the structural evolution of large volcanic edifices on the terrestrial planets. <https://doi.org/10.1144/SP401.7> (2015).
- Ma, K.-F., Kanamori, H. & Satake, K. Mechanism of the 1975 Kalapana, Hawaii, earthquake inferred from tsunami data. *J. Geophys. Res. Solid Earth* **104**, 13153–13167 (1999).
- Cervelli, P., Segall, P., Johnson, K., Lisowski, M. & Miklius, A. Sudden aseismic fault slip on the south flank of Kilauea volcano. *Nature* **415**, 1014–1018 (2002).
- Glicken, H. *Rockslide-Debris Avalanche of May 18, 1980, Mount St. Helens Volcano, Washington*. <https://pubs.usgs.gov/of/1996/0677/> (1996).
- Stoopes, G. R. & Sheridan, M. F. Giant debris avalanches from the Colima Volcanic Complex, Mexico: Implications for long-runout landslides (>100 km) and hazard assessment. *Geology* **20**, 299–302 (1992).
- Belousov, A., Belousova, M. & Voight, B. Multiple edifice failures, debris avalanches and associated eruptions in the Holocene history of Shiveluch volcano, Kamchatka, Russia. *Bull. Volcanol.* **61**, 324–342 (1999).
- Moore, J. G. et al. Prodigious submarine landslides on the Hawaiian Ridge. *J. Geophys. Res. Solid Earth* **94**, 17465–17484 (1989).
- Masson, D. G. et al. Slope failures on the flanks of the western Canary Islands. *Earth-Sci. Rev.* **57**, 1–35 (2002).
- van Wyk de Vries, B. & Francis, P. W. Catastrophic collapse at stratovolcanoes induced by gradual volcano spreading. *Nature* **387**, 387–390 (1997).
- Moore, J. G. & Moore, G. W. Deposit from a Giant Wave on the Island of Lanai, Hawaii. *Science* **226**, 1312–1315 (1984).
- Ward, S. N. & Day, S. Cumbre Vieja volcano—potential collapse and tsunamis at La Palma, Canary Islands. *Geophys. Res. Lett.* **28**, 3397–3400 (2001).
- Zorn, E. U. et al. Interactions of magmatic intrusions with the multiyear flank instability at Anak Krakatau volcano, Indonesia: Insights from InSAR and analogue modeling. *Geology* **51**, 340–344 (2023).
- Walter, T. R. et al. Complex hazard cascade culminating in the Anak Krakatau sector collapse. *Nat. Commun.* **10**, 1–11 (2019).
- Hürlimann, M., García-Piera, J. O. & Ledesma, A. Causes and mobility of large volcanic landslides: application to Tenerife, Canary Islands. *J. Volcanol. Geotherm. Res.* **103**, 121–134 (2000).
- del Potro, R. & Hürlimann, M. Geotechnical classification and characterisation of materials for stability analyses of large volcanic slopes. *Eng. Geol.* **98**, 1–17 (2008).
- Martí, J. Las Cañadas caldera, Tenerife, Canary Islands: a review, or the end of a long volcanological controversy. *Earth-Sci. Rev.* **196**, 102889 (2019).
- Cecchi, E., van Wyk de Vries, B. & Lavest, J.-M. Flank spreading and collapse of weak-cored volcanoes. *Bull. Volcanol.* **67**, 72–91 (2004).
- Heap, M. J. et al. Alteration-induced volcano instability at La Soufrière de Guadeloupe (Eastern Caribbean). *J. Geophys. Res. Solid Earth* **126**, e2021JB022514 (2021).
- Heap, M. J. et al. Hydrothermal alteration can result in pore pressurization and volcano instability. *Geology* **49**, 1348–1352 (2021).
- Daniel, I. & Ishai, O. *Engineering Mechanics of Composite Materials*. vol. 3 (Oxford University Press, 2006).

27. Gudmundsson, A. *Rock Fractures in Geological Processes*. (Cambridge University Press, 2011).
28. Gudmundsson, A. How local stresses control magma-chamber ruptures, dyke injections, and eruptions in composite volcanoes. *Earth-Sci. Rev.* **79**, 1–31 (2006).
29. Thiele, S. T., Cruden, A. R., Zhang, X., Micklethwaite, S. & Matchan, E. L. Reactivation of magma pathways: insights from field observations, geochronology, geomechanical tests, and numerical models. *J. Geophys. Res. Solid Earth* **126**, e2020JB021477 (2021).
30. Carracedo, J. C. et al. The 2021 eruption of the Cumbre Vieja volcanic ridge on La Palma, Canary Islands. *Geol. Today* **38**, 94–107 (2022).
31. Carracedo, J. C., Day, S. J., Guillou, H. & Gravestock, P. Later stages of volcanic evolution of La Palma, Canary Islands: Rift evolution, giant landslides, and the genesis of the Caldera de Taburiente. *GSA Bull.* **111**, 755–768 (1999).
32. Thiele, S. T., Cruden, A. R., Micklethwaite, S., Bunger, A. P. & Köpping, J. Dyke apertures record stress accumulation during sustained volcanism. *Sci. Rep.* **10**, 17335 (2020).
33. Ancochea, E. et al. Constructive and destructive episodes in the building of a young Oceanic Island, La Palma, Canary Islands, and genesis of the Caldera de Taburiente. *J. Volcanol. Geotherm. Res.* **60**, 243–262 (1994).
34. Ferrer, M. et al. Volcanic mega-landslides in Tenerife (Canary Islands, Spain) in “Volcanic Rocks: Proceedings of ISRM Workshop W2, Ponta Delgada, Azores”, 185–191 (Taylor and Francis Group, 2007). <https://doi.org/10.1201/NOE0415451406.ch24>.
35. Seisdedos, J., Ferrer, M. & González de Vallejo, L. I. Geological and geomechanical models of the pre-landslide volcanic edifice of Güimar and La Orotava mega-landslides (Tenerife). *J. Volcanol. Geotherm. Res.* **239–240**, 92–110 (2012).
36. Martín, G., Cáceres, L. & Rabaleta, J. M. *Nuevo Trazado De La Carretera TF-812, De Santa Cruz De La Palma a Los Llanos De Aridane-Anejo no. 4: GEOLOGÍA Y GEOTECNIA*. (1998).
37. Dinçer, I., Acar, A., Çobanoğlu, I. & Uras, Y. Correlation between Schmidt hardness, uniaxial compressive strength and Young’s modulus for andesites, basalts and tuffs. *Bull. Eng. Geol. Environ.* **63**, 141–148 (2004).
38. Heap, M. J. & Violay, M. E. S. The mechanical behaviour and failure modes of volcanic rocks: a review. *Bull. Volcanol.* **83**, 33 (2021).
39. Heap, M. J. et al. Towards more realistic values of elastic moduli for volcano modelling. *J. Volcanol. Geotherm. Res.* **390**, 106684 (2020).
40. Villeneuve, M. C. & Heap, M. J. Calculating the cohesion and internal friction angle of volcanic rocks and rock masses. *Volcanica* **4**, 279–293 (2021).
41. Hoek, E. & Brown, E. T. The Hoek–Brown failure criterion and GSI–2018 edition. *J. Rock Mech. Geotech. Eng.* **11**, 445–463 (2019).
42. Hoek, E. & Diederichs, M. S. Empirical estimation of rock mass modulus. *Int. J. Rock Mech. Min. Sci.* **43**, 203–215 (2006).
43. Lisjak, A. et al. Acceleration of a 2D/3D finite-discrete element code for geomechanical simulations using General Purpose GPU computing. *Comput. Geotech.* **100**, 84–96 (2018).
44. Hansen, A., Hemmer, P. & Pradhan, S. *The Fiber Bundle Model: Modeling Failure in Materials*. (Wiley, 2015).
45. Pierce, F. The weakest link theorems on the strength of long and of composite specimens. *Text Inst J* **17**, 355–368 (1926).
46. Raischel, F., Kun, F. & Herrmann, H. J. Fiber bundle models for composite materials. in *Conference on Damage in Composite Materials* (2006).
47. Hemmer, P. C. & Hansen, A. The distribution of simultaneous fiber failures in fiber bundles. *J. Appl. Mech.* **59**, 909–914 (1992).
48. Michlmayr, G., Cohen, D. & Or, D. Shear-induced force fluctuations and acoustic emissions in granular material. *J. Geophys. Res. Solid Earth* **118**, 6086–6098 (2013).
49. Hidalgo, R. C., Grosse, C. U., Kun, F., Reinhardt, H. W. & Herrmann, H. J. Evolution of percolating force chains in compressed granular media. *Phys. Rev. Lett.* **89**, 205501 (2002).
50. Turcotte, D. L., Newman, W. I. & Shcherbakov, R. Micro and macroscopic models of rock fracture. *Geophys. J. Int.* **152**, 718–728 (2003).
51. Moura, A., Lei, X. & Nishisawa, O. Prediction scheme for the catastrophic failure of highly loaded brittle materials or rocks. *J. Mech. Phys. Solids* **53**, 2435–2455 (2005).
52. Kawada, Y. & Nagahama, H. Cumulative Benioff strain-release, modified Omori’s law and transient behaviour of rocks. *Tectonophysics* **424**, 157–166 (2006).
53. Newman, W. I., Gabrielov, A. M., Durand, T. A., Phoenix, S. L. & Turcotte, D. L. An exact renormalization model for earthquakes and material failure statics and dynamics. *Phys. Nonlinear Phenom.* **77**, 200–216 (1994).
54. Cohen, D., Lehmann, P. & Or, D. Fiber bundle model for multiscale modeling of hydromechanical triggering of shallow landslides. *Water Resour. Res.* **45**, W10436 (2009).
55. Failletaz, J., Or, D. & Reiweger, I. Codetection of acoustic emissions during failure of heterogeneous media: New perspectives for natural hazard early warning. *Geophys. Res. Lett.* **43**, 1075–1083 (2016).
56. Pollen, N. & Simon, A. Estimating the mechanical effects of riparian vegetation on stream bank stability using a fiber bundle model. *Water Resour. Res.* **41**, W07025 (2005).
57. Reiweger, I., Schweizer, J., Dual, J. & Herrmann, H. J. Modelling snow failure with a fibre bundle model. *J. Glaciol.* **55**, 997–1002 (2009).
58. Pradhan, S., Hansen, A. & Hemmer, P. C. Crossover behavior in burst avalanches: Signature of imminent failure. *Phys. Rev. Lett.* **95**, 125501 (2005).
59. Walter, T. R. et al. Rift zone reorganization through flank instability in ocean island volcanoes: an example from Tenerife, Canary Islands. *Bull. Volcanol.* **67**, 281–291 (2005).
60. van Wyk de Vries, B. & Matela, R. Styles of volcano-induced deformation: numerical models of substratum flexure, spreading and extrusion. *J. Volcanol. Geotherm. Res.* **81**, 1–18 (1998).
61. Bak, P. & Chen, K. Self-organized criticality. *Sci. Am.* **264**, 46–53 (1991).
62. Carracedo, J. C. The Canary Islands: an example of structural control on the growth of large oceanic-island volcanoes. *J. Volcanol. Geotherm. Res.* **60**, 225–241 (1994).

Acknowledgements

The authors thank the staff at Parque Nacional Caldera de Taburiente for their generous support and hospitality during fieldwork. S.T. would also like to acknowledge several helpful conversations with Prof. Julia Morgan and Ass. Prof. Laurence Brassart during the early stages of this work. S.T. was supported by a Westpac Future Leaders Scholarship and an Australian Postgraduate Award. A.R.C. gratefully acknowledges support from the Australian Research Council Discovery Grant DP190102422. Thoughtful and constructive reviews by M. Heap, J. Ball and S. Poppe significantly improved the final version of the manuscript.

Author contributions

All authors (S.T.T., A.R.C. and S.M.) contributed to the conceptualisation, data acquisition, analysis, modelling and writing of this study.

Funding

Open Access funding enabled and organized by Projekt DEAL.

Competing interests

The authors declare no competing interests.

Additional information

Supplementary information The online version contains supplementary material available at <https://doi.org/10.1038/s43247-023-01046-3>.

Correspondence and requests for materials should be addressed to Samuel T. Thiele.

Peer review information *Communications Earth & Environment* thanks Michael Heap, Jessica Ball and Sam Poppe for their contribution to the peer review of this work. Primary handling editor: Joe Aslin. A peer review file is available.

Reprints and permission information is available at <http://www.nature.com/reprints>

Publisher’s note Springer Nature remains neutral with regard to jurisdictional claims in published maps and institutional affiliations.



Open Access This article is licensed under a Creative Commons Attribution 4.0 International License, which permits use, sharing, adaptation, distribution and reproduction in any medium or format, as long as you give appropriate credit to the original author(s) and the source, provide a link to the Creative Commons license, and indicate if changes were made. The images or other third party material in this article are included in the article’s Creative Commons license, unless indicated otherwise in a credit line to the material. If material is not included in the article’s Creative Commons license and your intended use is not permitted by statutory regulation or exceeds the permitted use, you will need to obtain permission directly from the copyright holder. To view a copy of this license, visit <http://creativecommons.org/licenses/by/4.0/>.

© The Author(s) 2023